Analytical modeling of the harmonic distortion caused by squeeze film damping in MEMS-based acoustic transducers

Anton MELNIKOV[1] , **Hermann A.G. SCHENK[1], Franziska WALL[2]**

[1] Bosch Sensortec GmbH, Knappsdorfer Straße 12, 01099 Dresden, Germany,
[3] Fraunhofer Institute for Photonic Microsystems IPMS, Maria-Reiche-Straße 2, 01109 Dresden, Germany

Corresponding author: Anton MELNIKOV, email: anton.melnikov@bosch-sensortec.com

Abstract Miniaturized microelectromechanical system (MEMS) microspeakers are currently trending in the development of acoustic transducers. When a transducer is scaled down to fit on a microelectronic chip, its physics differ from the macroscopic world, and some common modeling assumptions become invalid. One of the effects observed in MEMS microspeakers is nonlinear squeeze film damping. Understanding this effect is crucial as non-linearities in the speaker can result in harmonic distortion, which is highly regulated in audio applications. In this study, we analyze the influence of squeeze film damping on harmonic distortions using a lumped parameter model of a MEMS microspeaker. This leads to a nonlinear ordinary differential equation, and an approximate analytical solution for moderate non-linearities is obtained using homotopy. We present our solution strategy, including the resulting closed-form expression, and verify our findings against numerical solutions.

Keywords: audio, loudspeaker, simulation, modelling, reduced order model, nonlinear system.

1. Introduction

A microelectromechanical systems (MEMS) microspeaker is a miniaturized acoustic transducer that utilizes MEMS technology to produce sound. It is designed for applications where space constraints and power efficiency are critical, such as portable electronic devices and small-scale systems. In general designing a MEMS microspeaker incorporates multidomain physics on a microscopic scale, including structural vibrations, electrostatic fields, acoustics etc. In the analysis of mechanical vibrations within macroscopic world, fluid dynamic damping nonlinearities are typically ignored due to the small displacement amplitudes compared to the dimensions of the fluid domain. However, when dealing with MEMS-based microspeakers [1], such as the one shown in Fig. 1, the displacement amplitudes of the air-displacing structures (e.g., diaphragms or beams) are significant in relation to the dimensions of the enclosing cavities. The MEMS microspeaker approach considered in this work (see Fig. 1) uses lateral deflection of microactuators to create out-of-plane fluid flow. Microscopic air chambers are located between the actuators and connected to outer space by acoustic openings. The displacement of actuators changes the volume of the air chambers and generated air flow mimicking air displacement by a vibrating diaphragm.

This approach allows to minimize chip area requirements compared to total air displacement by high packaging density of lateral actuators [2, 3]. However, the high packing density comes at a cost, as the actuators displacement simultaneously changes the width of the air chamber and the nonlinear squeeze film force's impact on the micro-speaker's frequency response must be carefully considered. To facilitate this analysis, accurate lumped parameter models that account for the relevant damping mechanisms are essential. These models should also be compatible with similar modeling tools used for other aspects of device physics [4–6]. In this study, we utilize a relatively straightforward lumped parameter model based on Reynolds equation to address squeeze film damping [7].
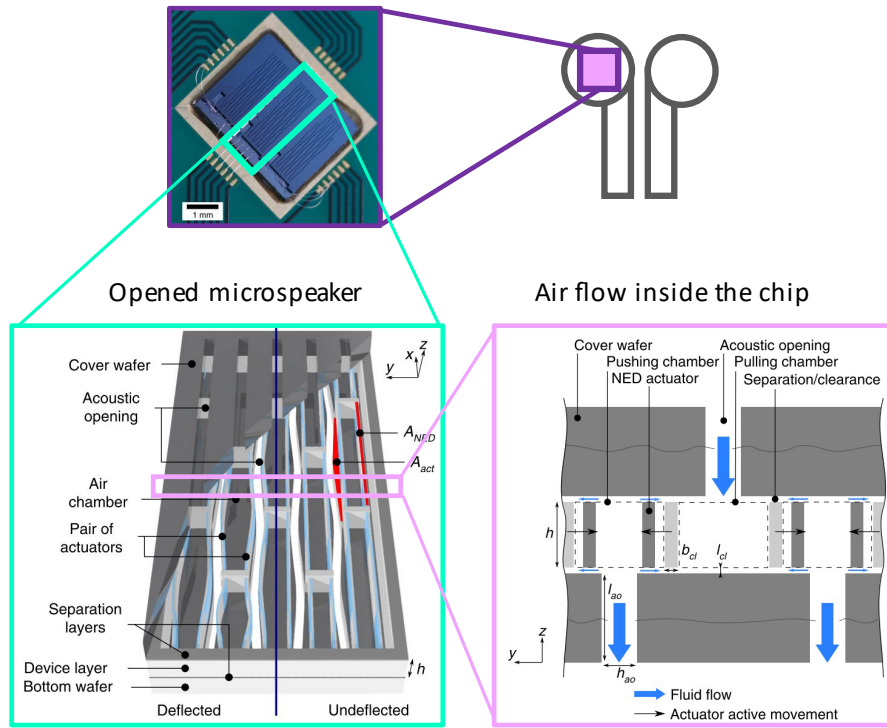
Figure 1. Exemplary MEMS microspeaker using lateral motion of actuators
for generating out-of-plane fluid flow (parts adopted from [1]).

2. Squeeze film damping

Squeeze film damping is a phenomenon resulting from the viscosity of a fluid that flows into and out of a volume bounded by two parallel plates as they move closer or farther apart. When the fluid between the plates can be considered incompressible, this non-linear behavior can be well described using the Reynolds equation:

$$\frac{\partial}{\partial x}\left(H^3 p \frac{\partial p}{\partial x}\right) + \frac{\partial}{\partial z}\left(H^3 p \frac{\partial p}{\partial z}\right) = 12\mu\left(H\frac{\partial p}{\partial t} + p\frac{\partial H}{\partial t}\right). \tag{1}$$

When introducing several simplifying assumptions, suitable for rigid parallel plates, this partial differential equation can be simplified to [7]

$$\frac{\partial^2 \Delta p}{\partial z^2} = \frac{12\mu}{H^3}\frac{\partial H}{\partial t}, \tag{2}$$

where Δp is the change in pressure, H is the gap size, and μ is the dynamic viscosity of the fluid. The squeeze film damping force acting on the actor, is given by the integral of this pressure over the actuator surface area

$$\Delta F(t) = \int_A \Delta p(z,t)\, dA. \tag{3}$$

In the following we consider the simplified setup shown in Fig. 2. A moving plate facing a fixed wall on left and right displaces air in two narrow slits with a single opening over the full length of the slit at $z = +\frac{w}{2}$ on the left and at $z = -\frac{w}{2}$ on the right. For example, at the left side this leads to the following boundary conditions for the air chamber [8]:

$$\Delta p\left(z = +\frac{w}{2}\right) = p_A,$$
$$\frac{\partial}{\partial z}\Delta p\left(z = -\frac{w}{2}\right) = 0,$$
$$\frac{\partial}{\partial z}\Delta p\left(x = +\frac{L}{2}\right) = 0,$$
$$\frac{\partial}{\partial z}\Delta p\left(x = -\frac{L}{2}\right) = 0. \tag{4}$$

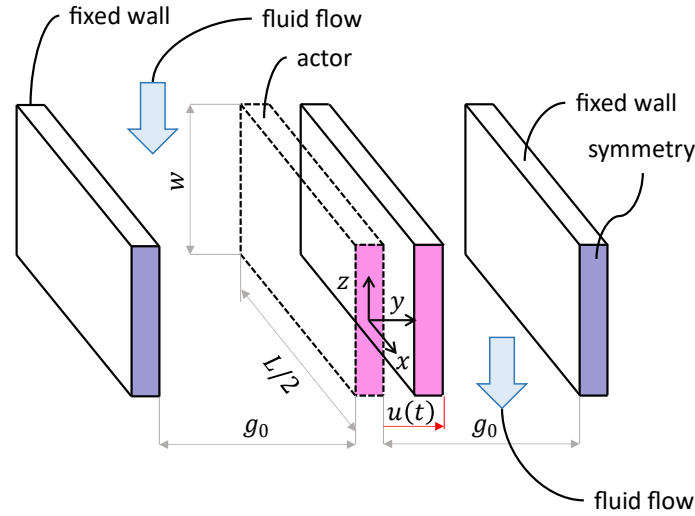Here p_A is an acoustic pressure at the slit opening.

Figure 2. Simplified microspeaker model with two air chambers and lateral displacement of the actor.

3. Nonlinearity of the damping force for a single air chamber

3.1. Harmonic distortions of the force

Using boundary conditions, the simplified Reynolds equation can be integrated, leading to the following force equation

$$\Delta F(t) = -\frac{4\mu w h^3 L}{H(t)^3}\frac{dH(t)}{dt}\,,\tag{5}$$

where L is the actor length and w is the actor height as shown in Fig. 2. To evaluate the damping force caused by an externally imposed harmonic movement, we assume a rigid actor and make the approach

$$H(t) = g_0 - \hat{u}\cos(\omega t)\,,\tag{6}$$

with g_0 as the initial gap and $\hat{u}$ as the amplitude of harmonic oscillation (see Fig. 2). This analysis solely considers the force response associated with a single-frequency harmonic motion, disregarding the presence of higher harmonics that arise in a nonlinear configuration. When the amplitudes are small and therefore the change of the slit height H (corresponds to the width of the air chamber) is negligible, we obtain a constant damping coefficient

$$c = \frac{4\mu L w^3}{g_0^3}\,,\tag{7}$$

as known from linear oscillator theory. As mentioned previously, in case of MEMS microspeakers with laterally moving actors, deflections beyond the scope of the linear theory may occur. To obtain the nonlinear damping force relevant to larger actuator movements, we insert Eq. (6) into Eq. (5) leading to

$$\Delta F(t) = -\frac{4\mu w^3 L \omega \delta}{g_0^2} f(t)\,,\tag{8}$$

with

$$f(t) = \frac{\sin(\omega t)}{(1 - \delta\cos(\omega t))^3}\,,\tag{9}$$

with the nondimensional normalized displacement amplitude $\delta = \frac{\hat{u}}{g_0}$.

When the MEMS actuator is exposed to the nonlinearity of a squeeze film damping force according to Eq. (8) and Eq. (9), the movement of it will be subjected to harmonic distortions. These damping force distortions will affect the acoustic pressure generated by the air displacement. To analyze the higher harmonics of the damping force, we expand $f(t)$ as a Fourier series

$$f(t) = \sum_{n=1}^{\infty} (a_n \cos(n\omega t) + b_n \sin(n\omega t)) \,. \tag{10}$$

The Fourier coefficients b_n are given by the integrals

$$b_n(\delta) = \frac{\omega}{\pi} \int_{-\frac{\pi}{\omega}}^{+\frac{\pi}{\omega}} \frac{\sin(n\omega t) \sin(\omega t)}{(1 - \delta \cos(\omega t))^3} dt \,, \tag{11}$$

and all a_n vanish due to symmetry. The b_n integrals can be analytically evaluated,

$$b_n(\delta) = n \frac{\left(1 + n\sqrt{1 - \delta^2}\right) \beta^{n-1}}{(1 - \delta^2)^{3/2}\left(1 + \sqrt{1 - \delta^2}\right)^n} \,. \tag{12}$$

The harmonic distortion is characterized by the harmonic distortion coefficients k_n, defined as the ratio between the higher harmonic amplitudes and the fundamental response amplitude

$$k_n(\delta) = \left| \frac{b_n}{b_1} \right| \,, \tag{13}$$

while in our case this leads to

$$k_n(\delta) = n \, \delta^{n-1} \frac{\left(1 + n\sqrt{1 - \delta^2}\right)}{\left(1 + \sqrt{1 - \delta^2}\right)^n} \,. \tag{14}$$

Subsequently, we use Parseval's theorem,

$$\frac{\omega}{\pi} \int_{-\frac{\pi}{\omega}}^{+\frac{\pi}{\omega}} f(t)^2 dt = \sum_{n=1}^{\infty} b_n(\delta)^2 \,, \tag{15}$$

and $b_1(\delta)$ to compute the harmonic distortion,

$$\text{THD}_{\text{SQFD}}(\delta) = \sqrt{1 - \frac{b_1(\delta)^2}{\sum_{n=1}^{\infty} b_n(\delta)^2}} = \sqrt{1 - \frac{4(1 - \delta^2)^{3/2}}{4 + 3\delta^2}} \,. \tag{16}$$

It needs to be mentioned that THD_{SQFD} is a pseudo THD, solely used here for characterizing the nonlinearity of the damping force. It does not capture the full dynamic response of the system. THD_{SQFD} is therefore, not apt for use in audio applications. The THD_{F} relevant for audio applications is addressed in the next section.

3.2. Proof of the closed-form expression with FEM

To validate the analytical model, we evaluated a numerical solution of the Reynolds equation using a two-dimensional finite element method (FEM) for rigid actuator plates. The simulation was implemented using COMSOL Multiphysics software. Figure 3 illustrates the damping force for a single time period (cosine-driven) at various δ values, computed both with FEM and using Eq. (9). It is evident that the curves from both approaches in Fig. 3 match each other. Thus, the model represented by Eq. (9) appears to establish a strong foundation for incorporating the effects described by the nonlinear Reynolds equation into lumped parameter models.

Regarding the impact of the squeeze film force on actuator dynamics, it is noteworthy that the normalized peak force between $\delta = 0$ and $\delta = 0.9$ increases by a factor of 121, while the peaks of the force amplitude progressively concentrate around the centre of the period (referred to as the "whiplash effect"). This shift in peak values can be attributed to the singular nature of the Reynolds model for the damping force, as indicated by Eq. (9), as δ approaches 1. It is important to note that the occurrence of a singular damping force, as predicted by the Reynolds equation (Eq. (1)), is unlikely to occur in reality, due to the presence of rarefaction (considering the Knudsen number) and the violation of the incompressibility assumption of the Reynolds equation beyond a certain amplitude of motion.

In Fig. 4a, we present a more detailed comparison by examining distortion coefficients k_n up to order 6. Consistent with previous findings, there is a generally strong agreement between the FEM simulation and the analytical curves. However, a minor discrepancy can be observed for the 5th and 6th harmonics at $\delta = 0.95$, particularly near the singularity. Although this slight deviation may raise questions about the accuracy of the FEM simulation in that region, it still supports the applicability of Eq. (9).

Consequently, Fig. 4a indicates that the nonlinear behavior of the damping force is predominantly governed by the nondimensional amplitude δ, which represents the displacement amplitude normalized by the gap. It is worth noting that the distortion coefficients k_n, as described in Eq. (14), are continuous and bounded functions throughout the entire range of $0 \leq \delta \leq 1$.
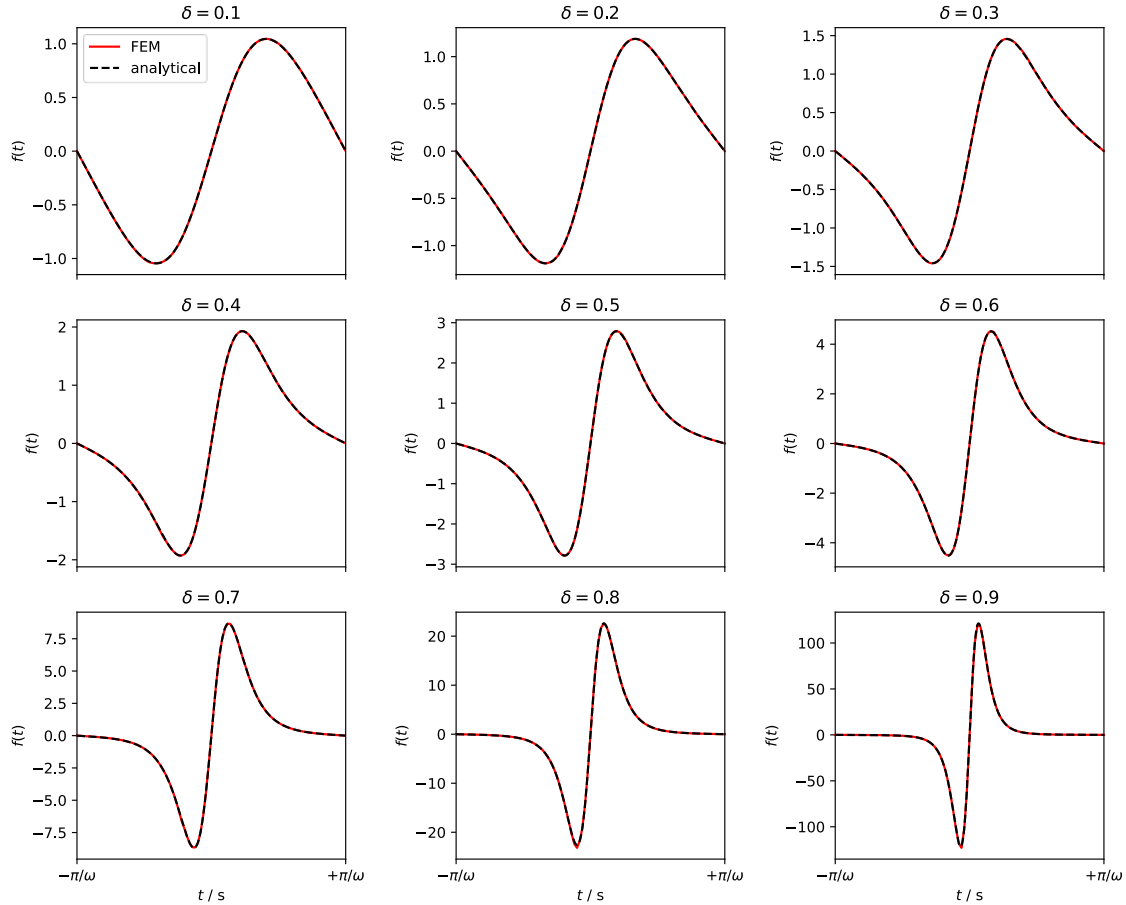

Figure 3. Time-dependent normalized damping force caused by the squeeze film for normalized amplitude δ. (Adopted from [8])
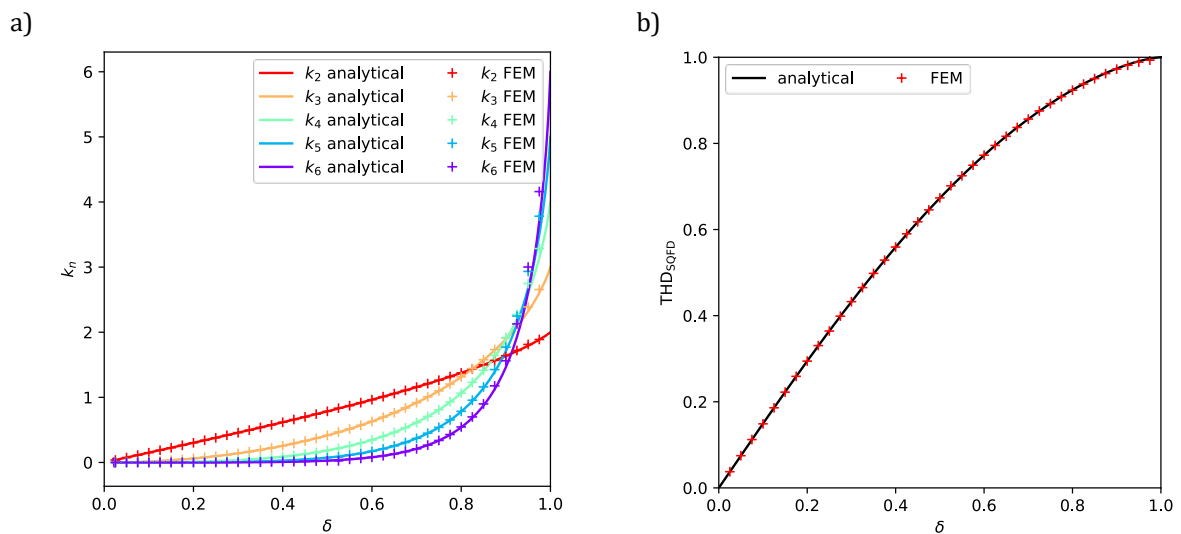
a)

b)

Figure 4. a) Distortion coefficients k_n up-to order 6 calculated using analytical expressions and FEM results. b) The THD_{SQFD} calculated using the analytical expression and by FEM. (Adopted from [8])

In particular, we have

$$0 \leq k_n(\delta) \leq k_n(1) = n. \tag{17}$$

Figure 4b illustrates the comparison between the $\mathrm{THD_{SQFD}}$ (pseudo THD) calculated using Eq. (16) and the corresponding FEM results. Once again, a strong agreement is observed between the two approaches. At $\delta = 1$, Eq. (16) yields $\mathrm{THD_{SQFD}} = 1$, and the FEM curve approaches 1 as δ approaches 1, although a direct evaluation at the singularity is not feasible with FEM. It should be noted that in this analysis, we employ the $\mathrm{THD_R}$ approach, which differs from the more commonly used $\mathrm{THD_F}$ in audio applications. They are related as [10]

$$\mathrm{THD_R} = \frac{\mathrm{THD_F}}{\sqrt{1 + \mathrm{THD_F^2}}}. \tag{18}$$

4. Nonlinear differential equation

In order to evaluate the nonlinear effects in a practical dynamic system, it is essential to analyze the system using oscillatory differential equations. The most basic form of such an equation of motion resulting from force equilibrium including the nonlinear damping force from Eq. (5) is

$$m \, \ddot{u}(t) + \frac{4 \, \mu \, w^3 L}{(g_0 - u(t))^3} \, \dot{u}(t) + k \, u(t) = F_{\mathrm{elec}}(t), \tag{19}$$

while the fluidic channel dimensions are shown in Fig. 2. Considering the air chambers inside a MEMS microspeaker of the lateral type [2, 9], see Fig. 1 and Fig. 2, squeeze film damping appears on both sides of the actuator. This results in a slightly modified equation of motion

$$m \, \ddot{u}(t) + 4 \, \mu \, w^3 L \left(\frac{1}{(g_0 - u(t))^3} + \frac{1}{(g_0 + u(t))^3} \right) \dot{u}(t) + k \, u(t) = F_{\mathrm{elec}}(t), \tag{20}$$

including two nonlinear damping terms with opposite signs in front of the deflection $u(t)$ in the denominator. The primary objective of this study is to derive a simplified analytical expression for the harmonic distortion described in Eq. (20) and validate its accuracy within the relevant parameter range through numerical solutions of the corresponding differential equation.

Our focus is on examining the harmonic distortion resulting from the squeeze film force. Specifically, we are interested in understanding the system's response when subjected to a purely harmonic driving force,

$$F_{\mathrm{elec}}(t) = F_0 \cos(\omega t). \tag{21}$$

It is important to note that in this scenario, the system will oscillate around zero deflection, meaning that the integral of $u(t)$ over a complete period will result in a zero value,

$$\int_0^T u(t) \, dt = 0, \quad T = \frac{2\pi}{\omega}. \tag{22}$$

By integrating the equation of motion Eq. (20) over a complete period and acknowledging that the squeeze film damping force can be expressed as a total time derivative, it becomes evident that the time average of the equation will result in zero. Another noteworthy observation pertaining to Eq. (20) is that it can solely generate odd harmonic distortions. This arises from the fact that $u(t)$ changes its sign whenever the driving force $F_{\mathrm{elec}}(t)$ undergoes a sign change.

Next we introduce the dimensionless quantities,

$$u(t) = \frac{F_0}{k} \, \xi(t), \qquad t = \frac{\tau}{\omega_0}, \qquad \nu = \frac{\omega}{\omega_0}, \qquad \zeta = \frac{1}{\sqrt{k \, m}} \frac{4\mu \, w^3 L}{g_0^{\,3}}, \qquad \delta = \frac{F_0}{k \, g_0}, \tag{23}$$

to bring our model into the much more convenient dimensionless form

$$\ddot{\xi}(t) + \zeta \left(\frac{1}{(1 - \delta \, \xi(t))^3} + \frac{1}{(1 + \delta \, \xi(t))^3} \right) \dot{\xi}(t) + \xi(t) = \cos(\nu\tau). \tag{24}$$

In this study, a numerical method is utilized to solve Eq. (24) using a standard ordinary differential equation (ODE) solver, such as the *solve_ivp* function from the SciPy library. The equation is solved step by step for each desired excitation frequency. After allowing sufficient time for transient effects to vanish (typically

around 80 oscillation periods), a steady-state segment of the oscillation is selected. The harmonic distortion is then extracted from this segment using numerical Fourier transform techniques.

In order to obtain an analytical approximation for the solution of this nonlinear parametric oscillator equation, we decompose $\xi(t)$ into homotopy series with respect to δ,

$$\xi(\tau) = \sum_{n=0}^{\infty} a_n(\tau)\, \delta^n \,. \tag{25}$$

By substituting this series into Eq. (24), we can expand both sides of the equation in terms of δ and equate the sum of coefficients for each power of δ to zero. Through this process, we find that all odd orders of the homotopy series must inevitably vanish,

$$a_{2n+1}(\tau) = 0 \,. \tag{26}$$

All even homotopy orders $a_{2n}(\tau)$ fulfil the equation of a linear harmonic oscillator, excited by specific driving forces $f_{2n}(\tau)$. The driving forces $f_{2n}(\tau)$ are dependent on the lower homotopy orders, meaning that $f_{2n}(\tau)$ depends on $a_{2k}(\tau)$ with $k < n$,

$$\ddot{a}_{2n}(\tau) + 2\,\zeta\,\dot{a}_{2n}(\tau) \,+\, a_{2n}(\tau) = f_{2n}(\tau) \,. \tag{27}$$

To be more specific, we will focus on the first three significant homotopy equations, each associated with their respective driving forces

$$f_0(\tau) = \cos(\nu\tau) \,, \tag{28}$$

$$f_2(\tau) = -4\,\zeta\,\frac{\partial}{\partial\tau}\,a_0(\tau)^3 \,, \tag{29}$$

$$f_4(\tau) = -6\,\zeta\,\frac{\partial}{\partial\tau}\bigl(a_0(\tau)^5 + 2\,a_0(\tau)^2 a_2(\tau)\bigr) \,. \tag{30}$$

As each of these driving forces can be expressed as the total time derivatives of periodic functions, we can deduce, as we did previously for the complete equation of motion, that the time average of each homotopy order will equate to zero, i.e.

$$\int_0^{\frac{2\pi}{\nu}} a_{2n}(\tau)\, d\tau = \, 0 \,. \tag{31}$$

By systematically solving the hierarchy of homotopy equations, beginning with the lowest order and incrementally progressing to higher orders, we can validate the aforementioned assertion that only odd harmonic orders are present. In summary, our homotopy computation reveals that $a_{2n}(\tau)$ represents a truncated Fourier series comprising solely odd harmonics up to the order of $2n + 1$,

$$a_{2n}(\tau) = \sum_{k=0}^{\infty}\bigl(\hat{a}_{2n,2k+1} \cos\bigl((2k+1)\nu\tau\bigr) + \hat{b}_{2n,2k+1} \sin\bigl((2k+1)\nu\tau\bigr)\bigr) \,. \tag{32}$$

The respective Fourier coefficients are obtained through a hierarchy of low-dimensional linear algebraic equations. Using these derived results, we can further determine the harmonic decomposition of the deflection $\xi(\tau)$,

$$\xi(\tau) = \sum_{j=0}^{\infty}\bigl(\hat{A}_{2j+1} \cos\bigl((2j+1)\nu\tau\bigr) + \hat{B}_{2j+1} \sin\bigl((2j+1)\nu\tau\bigr)\bigr) \tag{33}$$

$$\hat{A}_{2j+1} = \sum_{n=j}^{\infty} \hat{a}_{2n,2j+1}\, \delta^{2n} \,, \qquad \hat{B}_{2j+1} = \sum_{n=j}^{\infty} \hat{b}_{2n,2j+1}\, \delta^{2n} \,. \tag{34}$$

The total harmonic distortion THD_{F} is then defined as

$$\text{THD}_{\text{F}} = \sqrt{\sum_{j=1}^{\infty} k_{2j+1}^{\,2}} \,, \tag{35}$$

where the harmonic coefficients are given by

$$K_{2j+1} = \sqrt{\hat{A}_{2j+1}^{\;2} + \hat{B}_{2j+1}^{\;2}}, \qquad k_{2j+1} = \frac{K_{2j+1}}{K_1}. \tag{36}$$

In practical scenarios, K_3 significantly dominates the higher harmonics. Specifically, in cases where $\delta < 1$ and $\zeta < 1$, the primary contribution to this harmonic arises from the second homotopy order. This implies of course the main observation underlying this study

$$\text{THD}_\text{F} \approx k_3(\nu). \tag{37}$$

All occasionally lengthy analytical calculations were conducted utilizing the assistance of the Mathematica™ computer algebra system. The obtained Fourier coefficients, derived from the series expansion of $\xi(\tau)$ up to the $O[\delta]^2$ order, are as follows

$$\hat{A}_1 = \frac{1-\nu^2}{1-(2-4\zeta^2)\nu^2+\nu^4} + \frac{12\zeta^2\nu^2(-1+\nu^2)}{(1-(2-4\zeta^2)\nu^2+\nu^4)^3}\delta^2 + O[\delta]^4, \tag{38}$$

$$\hat{B}_1 = \frac{2\zeta\nu}{1-(2-4\zeta^2)\nu^2+\nu^4} + \frac{3\zeta\nu(1-2(1+2\zeta^2)\nu^2+\nu^4)}{(1-(2-4\zeta^2)\nu^2+\nu^4)^3}\delta^2 + O[\delta]^4, \tag{39}$$

$$\hat{A}_3 = -\frac{12\zeta^2\nu^2(3-21\nu^2-20\zeta^2\nu^2+33\nu^4+36\zeta^2\nu^4-15\nu^6)}{(1-(2-4\zeta^2)\nu^2+\nu^4)^3(1-(2-4\zeta^2)(3\nu)^2+(3\nu)^4)}\delta^2 + O[\delta]^4, \tag{40}$$

$$\hat{B}_3 = \frac{3\zeta\nu(1-12\nu^2-48\zeta^2\nu^2+30\nu^4+192\zeta^2\nu^4+48\zeta^4\nu^4-28\nu^6-144\zeta^2\nu^6+9\nu^8)}{(1-(2-4\zeta^2)\nu^2+\nu^4)^3(1-(2-4\zeta^2)(3\nu)^2+(3\nu)^4)}\delta^2 + O[\delta]^4. \tag{41}$$

This leads to the harmonic coefficients K_1 and K_3,

$$K_1 = \frac{1}{\sqrt{1-(2-4\zeta^2)\nu^2+\nu^4}} - \frac{6\zeta^2\nu^2}{(1-(2-4\zeta^2)\nu^2+\nu^4)^{5/2}}\delta^2 + O[\delta]^4, \tag{42}$$

and

$$K_3 =$$
$$\frac{3\zeta\nu}{(1-(2-4\zeta^2)\nu^2+\nu^4)^{3/2}\sqrt{1-(2-4\zeta^2)(3\nu)^2+(3\nu)^4}}\delta^2 \quad +$$
$$\frac{9\zeta\nu(5-100\nu^2-136\zeta^2\nu^2+590\nu^4+720\zeta^2\nu^4-2160\zeta^4\nu^4-900\nu^6-2376\zeta^2\nu^6+405\nu^8)}{8(1-(2-4\zeta^2)\nu^2+\nu^4)^{7/2}(1-(2-4\zeta^2)(3\nu)^2+(3\nu)^4)^{3/2}}\delta^4 + \tag{43}$$
$$O[\delta]^6.$$

Upto $O[\delta]^4$ this means for $k_3(\nu)$,

$$k_3(\nu) =$$
$$\frac{3\nu\zeta}{(1-(2-4\zeta^2)\nu^2+\nu^4)\sqrt{1-(2-4\zeta^2)(3\nu)^2+(3\nu)^4}}\delta^2 +$$
$$\frac{9\nu\zeta(5-100\nu^2-120\zeta^2\nu^2+590\nu^4+432\zeta^2\nu^4-1584\zeta^4\nu^4-900\nu^6-1080\zeta^2\nu^6+405\nu^8)}{8(1-(2-4\zeta^2)\nu^2+\nu^4)^3\;(1-(2-4\zeta^2)(3\nu)^2+(3\nu)^4)^{3/2}}\delta^4 + \tag{44}$$
$$O[\delta]^6$$

From this we conclude that the homotopy calculations combined with Eq. (37) provide a concise and surprisingly accurate approximation formula

$$\text{THD}_\text{F} \approx \frac{3\nu\zeta}{(1-(2-4\zeta^2)\nu^2+\nu^4)\sqrt{1-(2-4\zeta^2)(3\nu)^2+(3\nu)^4}}\delta^2 + O[\delta]^4, \tag{45}$$

which can be seen as a kind of main takeaway from this paper.

In this study, higher homotopy orders were computed; however, they did not yield significant improvements. It is important to note that the convergence of a homotopy series is highly dependent on the chosen deformation for analysis, which is particularly significant for non-linear parametric oscillators, as examined in this study. More advanced methods are available for analyzing the complex dynamics typically exhibited by parametric systems. Nevertheless, our simplified approach is justified due to the high accuracy and utility of the derived formula, Eq. (45).

5. Numerical solution vs. homotopy: variation of ζ

The squeeze film constant ζ, as defined in Eq. (23), represents the damping factor of the linearized system. This relationship is also evident from the homotopy equation Eq. (27). The damping factor is directly linked to the oscillator's quality factor Q through the equation

$$\zeta = \frac{1}{2Q}. \tag{46}$$

For loudspeakers, textbooks typically recommend quality factor values ranging from $Q = 0.25$ to $Q = 1.5$. In the subsequent analysis, we will confine ourselves to this specific parameter range. Furthermore, in this section, we choose $\delta = \frac{1}{4}$ to specifically examine the impact of the damping parameter ζ.

Figure 5 illustrates the outcomes for the normalized deflection amplitude ξ and the third harmonic distortion coefficient k_3, with a comparison between the numerical results and the zeroth-order homotopy results in Fig. 5 a,c. Regarding the amplitude ξ obtained from the homotopy approach (solid lines), it matches the response of a linear oscillator. Analyzing the amplitudes alongside the numerical results reveals that the nonlinearity significantly affects the curves primarily at resonance and for high quality factors (low ζ) within the selected range. The numerical and zeroth-order homotopy results exhibit good agreement for ζ values up to 0.82. However, even for the highest $\zeta = 1.5$, a slight discrepancy between the curves remains evident, as seen in the red solid line around $\nu = 0.2$ in Fig. 5a. Figure 5c demonstrates the third harmonic distortion coefficient k_3, which necessitates at least a second-order homotopy for its calculation (K_3). As the damping ζ increases, the response transitions from a double-humped band-pass curve to a single-peaked curve. The double-hump pattern arises only for lower ζ values, with the lower hump positioned near $\nu = \frac{1}{3}$, corresponding to a subharmonic resonance. Increasing the damping parameter ζ leads to a reduction in the frequency of the peak, and the hump associated with the actual resonance at $\nu = 1$ vanishes completely, with the sub-harmonic peak dominating for $\zeta > 0.52$.

Figure 5 c,d presents the outcomes, incorporating the second homotopy order in K_1 and the forth homotopy order in k_3. Overall, the analytically calculated amplitudes exhibit good agreement with the numerically calculated ones, with a slight deviation observed at the resonance for $\zeta = 0.33$. However, a notable discrepancy would arise at the resonance if ζ were further decreased. The results for k_3, obtained through the second-order homotopy (Fig. 5d), do show an improvement compared to the second-order homotopy (Fig. 5c). This outcome demonstrates that the homotopy approach offers user-friendly expressions that prove adequate for practical applications when $\zeta > 0.33$ (refers to $Q < 1.5$). Nevertheless, this finding is specifically valid for $\delta \le \frac{1}{4}$, and the impact of this parameter warrants further investigation in subsequent steps.
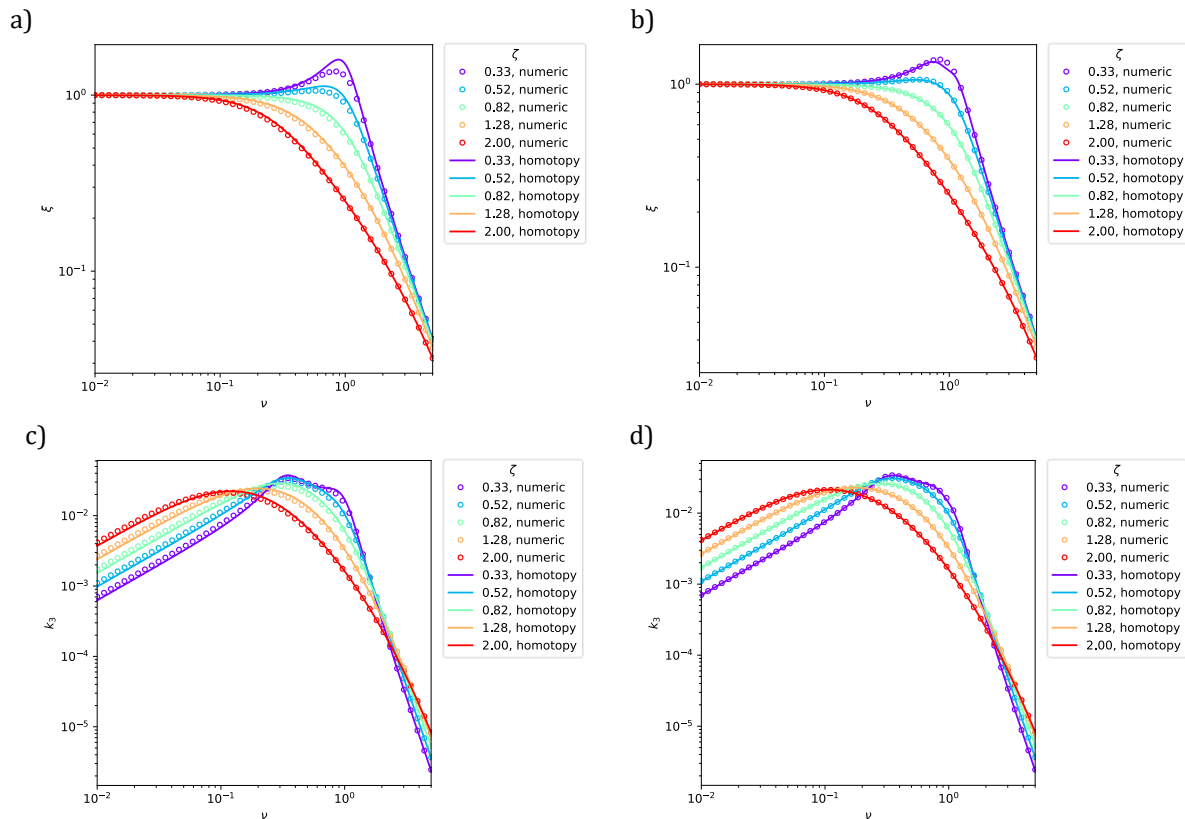
Figure 5. Numerical and analytical results for different ζ and $\delta = \frac{1}{4}$. Deflection amplitude ξ using (a) zeroth-order and (b) second-order homotopy. Dominant THD$_F$ component k_3 using (c) second-order and (d) fourth-order homotopy.

6. Numerical solution vs. homotopy: variation of δ

In this section, we set $\zeta = 0.52$, which corresponds to typical values for loudspeakers. Meanwhile, we vary the parameter δ (as defined in Eq. (23)) within the range of 0.1 to 0.9. According to the definition in Eq. (23), a value of $\delta = 0.1$ implies that in the quasi-static case with $\nu \to 0$, the physical deflection $u(\tau)$ under the force F_0 would be $0.1g_0$, and correspondingly, $\delta = 0.9$ results in $0.9g_0$. Therefore, the feasible region is defined as $0 \leq \delta < 1$, as $\delta \geq 1$ would yield unphysical results within the scope of this model.

Figure 6a presents a comparison of amplitude results obtained from numerical and analytical solutions using the zeroth-order homotopy. It is important to note that in this scenario, the homotopy approach yields a linear harmonic oscillator that remains unaffected by variations in δ. Consequently, the homotopy solution aligns with the numerical results for small values of δ, while as δ increases, the numerical curves deviate significantly from the homotopy. This discrepancy is particularly pronounced in the range from $\nu = 10^{-1}$ to $\nu = 1$. The results for k_3 are displayed in Fig. 6c, where a high level of accuracy is observed between the numerical and homotopy results for $\delta = 0.1$. Although the accuracy is still acceptable for $\delta = 0.26$ (blue color), the results become less accurate starting from $\delta = 0.42$ (aquamarine color). Notably, for larger values of δ, the qualitative behavior of the numerical results undergoes significant changes that are not captured by low-order homotopy.

The inclusion of second-order homotopy coefficients in K_1 does not necessarily lead to a more accurate solution, as can be observed in Fig. 6b. However, for $\delta = 0.26$, the homotopy curve (blue solid line) exhibits better alignment with the numerical results compared to Fig. 6a. For values of δ greater than 0.26, a distinct notch at resonance begins to emerge, growing in prominence as δ increases. This behavior is not reflected in the numerical results and is thus considered inaccurate. The results for k_3 using second-order homotopy are presented in Fig. 6d. While spurious notches are observed at $\nu \approx \frac{1}{3}$ and $\nu \approx 1$ for higher values of δ, the

results show significant improvement for $\nu < \frac{1}{3}$, particularly evident for $\delta = 0.42$ (aquamarine line, Fig. 6c vs. Fig. 6d) and $\delta = 0.58$ (light-green line Fig. 6c vs. Fig. 6d).
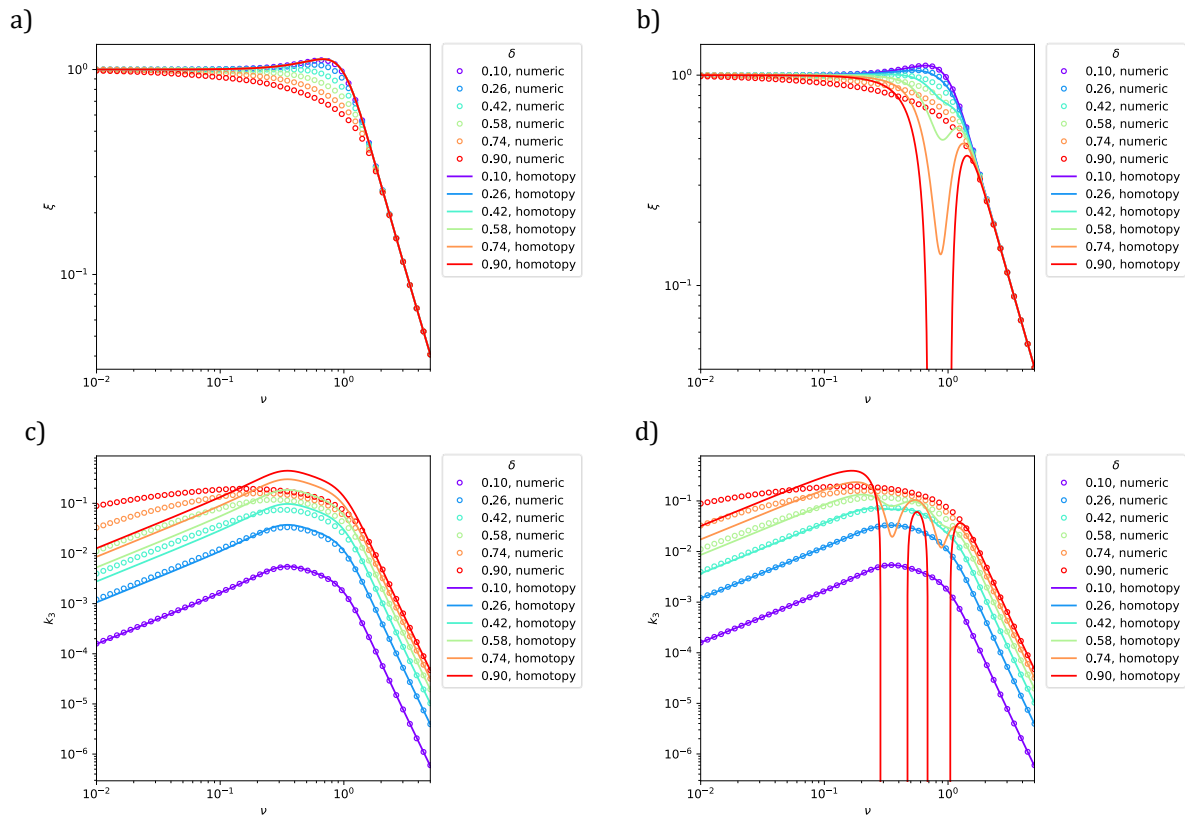

Figure 6. Numerical and analytical results for different ξ and $\zeta = 0.52$. Deflection amplitude ξ using (a) zeroth-order and (b) second-order homotopy. Dominant THD_F component k_3 using (a) second-order and (d) fourth-order homotopy.

7. Conclusion

In this study, we have examined the impact of nonlinear squeeze film damping on simplified a MEMS microspeaker using a lumped parameter model. We have demonstrated that this model, which incorporates damping nonlinearity, can be condensed and fully characterized by the parameters ζ and δ. Through a homotopy approach, we have derived remarkably accurate closed-form expressions for K_1, K_3 and subsequently THD_F, offering practical utility. Numerical solutions of Eq. (24) have provided valuable insights into the system's behavior across a technically relevant range of ζ and δ. Comparing the second-order homotopy results with the numerical solutions has revealed good agreement for $\zeta \geq 0.52$ ($Q \leq 0.96$) and $\delta \leq 0.26$. However, further research is needed to obtain accurate analytical expressions for an extended parameter range, including $\zeta < 0.52$ and $\delta > 0.26$.

Additional information

The author(s) declare: no competing financial interests and that all material taken from other sources (including their own published works) is clearly cited and that appropriate permits are obtained.

References

1. H. Wang, Y. Ma, Q. Zheng, K. Cao, Y. Lu, H. Xie; Review of Recent Development of MEMS Speakers; Micromachines, 2012, 12(10), 1257
2. B. Kaiser, S. Langa, L. Ehrig, M. Stolz, H. Schenk, H. Conrad, H. Schenk, K. Schimmanz, D. Schuffenhauer; Concept and proof for an all-silicon MEMS micro speaker utilizing air chambers; Microsystems & Nanoengineering, 2019, 5(1), 1–11

3. J. M. Monsalve, et al.; Proof of concept of an air-coupled electrostatic ultrasonic transducer based on lateral motion; Sensors and Actuators A: Physical, 2022, 345, 113813

4. A. Melnikov, H. A. G. Schenk, J. M. Monsalve, F. Wall, M. Stolz, A. Mrosk, S. Langa, B. Kaiser; Coulomb-actuated microbeams revisited: experimental and numerical modal decomposition of the saddle-node bifurcation; Microsystems & Nanoengineering, 2021, 7(1), 41

5. J. M. Monsalve, A. Melnikov, B. Kaiser, D. Schuffenhauer, M. Stolz, L. Ehrig, H. Schenk, H. Conrad, H. Schenk; Large-Signal Equivalent-Circuit Model of Asymmetric Electrostatic Transducers; IEEE/ASME Transactions on Mechatronics, 2022, 27(5), 2612–2622

6. H. A. Schenk, A. Melnikov, F. Wall, M. Gaudet, M. Stolz, D. Schuffenhauer, B. Kaiser; Electrically Actuated Microbeams: An Explicit Calculation of the Coulomb Integral in the Entire Stable and Unstable Regimes Using a Chebyshev-Edgeworth Approach; Physical Review Applied, 2022, 18(1), 014059; DOI: 10.1103/PhysRevApplied.18.014059

7. M. Bao, H. Yang; Squeeze film air damping in MEMS; Sensors and Actuators A: Physical, 2027, 136 (1), 3–27

8. A. Melnikov, H. A. G. Schenk, F. Wall, B. Kaiser; Nonlinear damping effects in MEMS-based microspeakers; Proceedings of the 24th International Congress on Acoustics, ICA2022, Gyeongju, Korea, October 24–28, 2022

9. B. Kaiser, H. A. G. Schenk, L. Ehrig, F. Wall, J. M. Monsalve, S. Langa, M. Stolz, A. Melnikov, H. Conrad, D. Schuffenhauer, H. Schenk; The push-pull principle: an electrostatic actuator concept for low distortion acoustic transducers, Microsystems & Nanoengineering, 2022, 8(125); DOI: 10.1038/s41378-022-00458-z

10. D. Shmilovitz; On the definition of total harmonic distortion and its effect on measurement interpretation; IEEE Transactions on Power Delivery, 2005, 20(1), 526–528